DOI: 10.1002/((please add manuscript number))

Article type: Communication

Direct visualization of reversible O^{2-}/O^{-} redox process in Li-rich cathode materials

Xiang Li, Yu Qiao, Shaohua Guo, Zhenming Xu, Hong Zhu, Xiaoyu Zhang, Yang Yuan, Ping He,* Masayoshi Ishida, and Haoshen Zhou**

X. Li, Prof. S. H. Guo, X. Y. Zhang, Y. Yuan, Prof. P. He, Prof. H. S. Zhou

Center of Energy Storage Materials & Technology, College of Engineering and Applied Sciences, National Laboratory of Solid State Microstructures, and Collaborative Innovation Center of Advanced Microstructure

Nanjing University

Nanjing 210093, China

E-mail: shguo@nju.edu.cn

pinghe@nju.edu.cn

hszhou@nju.edu.cn

Z. Xu, Prof. H. Zhu,

University of Michigan-Shanghai Jiao Tong University Joint Institute

Shanghai Jiao Tong University

Shanghai 200240, China

X. Li, Y. Qiao, Prof. M. Ishida

Graduate School of System and Information Engineering

University of Tsukuba

Tennoudai 1-1-1, Tsukuba, 305-8573, Japan

X. Li, Prof. S. H. Guo, Prof. H. S. Zhou

Energy Technology Research Institute

National Institute of Advanced Industrial Science and Technology (AIST)

Umezono 1-1-1, Tsukuba 305-8568, Japan.

Keywords: Li-ion batteries, Li-rich material, oxygen redox, in-situ XRD, in-situ Raman

Abstract: Conventional cathodes of Li-ion batteries mainly operate through an insertion-extraction process involving transition metal redox. These cathodes cannot meet the increasing requirements until lithium-rich layered oxides emerge with beyond-capacity performance. Nevertheless, in-depth understanding of the evolution of crystal and excess capacity delivered by Li-rich layered oxides is insufficient. Herein, we employ the various in-situ technologies such as X-ray diffraction (XRD) and Raman spectroscopy for a typical material $Li_{1.2}Ni_{0.2}Mn_{0.6}O_2$, directly visualizing O^--O^- (peroxo oxygen dimers) bonding mostly along the *c*-axis and demonstrating reversible O^{2-}/O^- redox process. Additionally, the formation of peroxo O-O bond is calculated via the density functional theory (DFT), and the corresponding O-O bond length of ~1.3 Å matches well with in-situ Raman results. These findings enrich the oxygen chemistry in layered oxides and open opportunities to design the high-performance positive electrodes for lithium-ion batteries.

Introduction:

The applications of Lithium-ion batteries (LIBs) like mobile devices are familiar in our daily lives.[1] However, the energy density of nowaday LIBs is still unsatisfying toward our increasing requirements.[2, 3] The most common positive electrodes, such as $LiCoO_2$, $LiFePO_4$, and $LiMn_2O_4$, are

still limited to the unsatisfied capacity, hindering the development of LIBs.[4] To allay the gap between supply and demand, we should settle the capacity issue. Therefore, aiming at improving the battery performance, a lot of efforts have been made in searching for better electrode materials with high capacity and good cyclic ability.[5]

Recently, lithium-rich layered oxides like $Li_{1.2}Ni_{0.166}Co_{0.067}Mn_{0.567}O_2$ with higher capacities than 250 mA h g^{-1} were reported.[6] These Li-rich materials can deliver excess capacity beyond the theoretical capacity based on cationic redox process, having received worldwide attention. The compounds (1-x)$LiNi_{0.5}Mn_{0.5}O_2$·xLi_2MnO_3, which can be also written as $Li[Li_{(1-2x)/3}Ni_xMn_{(2-x)/3}O_2]$, are well known.[7, 8] However, the mechanism based on cationic redox process is unable to explain the anomalous capacities exhibited by Li-rich materials. Thus, another new process, oxygen activation has been proposed to account for the phenomenon. Luo *et al.* pointed out that localized electron holes are formed on oxygen ions with the configuration surrounding by Mn^{4+} and Li^+ in $Li_{1.2}[Ni_{0.13}Co_{0.13}Mn_{0.54}]O_2$.[9] Seo *et al.* depicted that oxygens are easily oxidized due to the Li-O-Li configuration.[10] Sathiya *et al.* observed the peroxo-like species formed reversible in $Li_2Ru_{1-y}Sn_yO_3$.[11] However, all above-mentioned results are lacking in direct especially in-situ evidence for deep insight into the microstructure evolution of Li-rich layered oxides. McCalla *et al.* visualized the O-O dimers via TEM and neutron powder diffraction by using Li_2IrO_3 as a model compound and determined the possible limits on the value of *n* for peroxo-like O_2^{n-} dimers (the lower bound *n*=3 and the upper *n*=3.3), leading to a further understanding of anionic redox process.[12] Here, we focus on the representative material $Li_{1.2}Ni_{0.2}Mn_{0.6}O_2$ and investigate its charge-discharge processes during initial cycles by in-situ XRD and in-situ Raman spectroscopy. We demonstrate the structural change by the continuous shift of *c*-parameter and the direct evidence of peroxo O-O bond formation and

extinction (O_2^{2-} dimers). What's more, the well reversible formation/extinction of the dimers can be clearly observed in subsequent cycles, accompanied with synchronous structural change. Moreover, we can speculate that the peroxo O-O bond is along the *c*-axis by combining the variation trend of *c* lattice and peroxo O-O bond distance. Our findings provide a direct and new evidence for the reversible anionic redox chemistry in Li-rich cathode materials and a guideline towards designing the next generation of cathode materials with both cationic and anionic reversible redox process which can deliver substantially high energy density.

The compound was characterized by powder XRD and scanning electron microscopy (SEM) in **Figure 1**a and **1**b. $Li_{1.2}Ni_{0.2}Mn_{0.6}O_2$ is derived from Li_2MnO_3 by using Ni^{2+} to replace partial Li^+ and Mn^{4+} in transition metal (TM) layers. The XRD pattern indicates that most of the diffraction lines can be well indexed to a monoclinic Li_2MnO_3-like structure with space group C2/m.[13] Rietveld refinements of the XRD pattern obtained by GSAS + EXPGUI suite[14] successfully give reasonably low χ^2 (2.72) value based on Li_2MnO_3 model. The calculated XRD patterns have a good match with experimental data. The detailed refinement results are shown in the Table S17 (Supporting Information). SEM images in **Figure 1**b reveal that spheroidal particles with a diameter of around 8 μm are secondary particles formed from primary nanocrystals. The morphology of the particles is inherited from their hydroxide precursors (Figure S1, Supporting Information).

The electrochemical tests of as-prepared cathode were performed galvanostatically within the potential window (vs Li/Li^+) of 2.0 V ~ 4.7 V using 5 mA g^{-1}. **Figure 1**c shows the results during the first two cycles and corresponding dQ/dV curves can be seen in Figure S2 (Supporting Information). During the first charging process, the peaks located at ~ 3.75 V and 4.2 V are ascribed to the separate oxidation of nickel. The slope and plateau in initial charging process relate to the different

Li^+ extraction processes. It is easy to see the capacity of first charging is 350 mA h g^{-1}, indicating there are more than 1.1 Li^+ removed from the structure. It is worth noting that there are only 0.4 Li^+ can be removed when Ni^{2+} is totally oxidized to Ni^{4+}, corresponding ~ 130 mA h g^{-1} at this point, far less than 350.[3, 8, 15] The capacity of first discharging is ~ 287 mA h g^{-1}, indicating that there are about 0.9 Li^+ reinserted into the structure, leading to about 0.2 Li^+ loss. **Figure 1**d presents the cycling performance and coulombic efficiency. The capacity retention of the cathode at 25 mA g^{-1} after 50 cycles is 90.90% with limited capacity decay. If we focus on cations in this composition, capacity will only come from Ni-based redox process because of electrochemical inertness of Mn^{4+}.[4] As mentioned above, it is available to understand the relationship between the excess capacity and the evolution of the structure.

To unveil the lithiation-delithiation mechanism in $Li_{1.2}Ni_{0.2}Mn_{0.6}O_2$ during cycling processes, in-situ XRD was performed for the initial two cycles, displayed in **Figure 2** and Figure S4 (Supporting Information). The XRD pattern of cathode material assembled in the in-situ cell before test is shown in Figure S3 (Supporting Information). For the reason of structural similarity between Li_2MnO_3 and $LiNi_{0.5}Mn_{0.5}O_2$, in-situ XRD patterns can be fitted to hexagonal unit cell for convenience.[16] As it can be seen, the peak position, such as (003) and (104), changes regularly with the process of charging and discharging, representing reversible Li-ion insertion-extraction during the test. (003) peak directly reflects the evolution of *c* lattice parameter of the compound. Therefore, it can be used for further understanding of the phase transformation mechanism in the system. As seen in **Figure 2**, at the beginning of the first charging, (003) peak shifts to the left continuously then gradually shifts back to the high angle region till the end of charging. The electrochemical record shows the turning point of (003) shifting is around 4.5 V. It means *c* lattice value increases at first until the voltage

reaches to 4.5 V, followed by a sequential decrease. During discharging, reversed shift compared to the charging process is obvious. The evolution of (003) peak shifting within the first two cycles can be seen clearly in color graph in **Figure 2**. More importantly, this tendency of (003) shifts during the second cycle is similar to the first cycle.

The Rietveld refinement of *a* and *c* lattice parameters for the structure together with corresponding unit cell volume changing during the first two cycles are displayed in **Figure 2** and Figure S5 (Supporting Information). **Figure 2** discloses the *a*-lattice parameter continuously decrease whereas *c*-lattice parameter increases at the beginning and then decreases during the charge steps. At the beginning, the reduced ionic radii in TM layers may be the reason why *a*-parameter decreases.[4] The extraction of Li^+ from the Li-layers is accompanied by the increasing electrostatic repulsion between oxygen slabs, making an extendibility of unit cell along *c*-axis, corresponding to the shift of (003) to lower angles.[17] And then, the *c*-parameter and *a*-parameter change smoothly, indicating that some different reactions appear in this region. And during this region, Li^+ begins to extract from the TM slabs, leading the inverse changes of unit cell and shifting (003) peak to higher reflection angles. The variation is consistent with the previous work.[18] During discharge, the reversed shift of the (003), (104) peak can be observed, indicating some opposite processes happens compared with charging. Notably, the changes of the peaks' position during the 2nd cycle are analogous to the first cycle, representing the parallel lithiation-delithiation mechanism, which coincides with the discussion above.

Recently, the observation of higher capacity in relevant systems tends to be ascribed to the oxygen-related anionic electrochemical process.[9, 19, 20] Thus, as a powerful tool to investigate the oxygen redox behaviors, [21, 22] in-situ Raman has been employed (**Figure 3,** wider Raman Shift region

is shown in Figure S6, Supporting Information). In order to collect shell-isolated nanoparticle-enhanced Raman (SHINER) signal, gold nanoparticles (NPs) approximately 40 nm in diameter with a SiO_2 coating shell (~5 nm) were synthesized as in previous reports.[23] The washed and dried Au@SiO_2 NPs were dripped onto the specific cathode surface and vacuum dried before assembly. Regardless of the detailed analysis on overlapping stretching modes in MO_6 octahedron (below 700 cm^{-1}),[24] the variation trend of several novel peaks become noteworthy during cycling. One sharp peak can be observed at 953 cm^{-1} once the potential climbs up to 4.4 V, which is due to the adsorption of the anion in perchlorate salt (ClO_4^- symmetric stretching). [22] The related peak intensity quickly reaches maximum value due to the saturation of adsorption on the cathode surface. Besides, the unique adsorption feature can be further proved by the potential-dependent dropping trend during discharging (see more details in Figure S7, Supporting Information). More importantly, within the typical peroxo O-O stretch region (700-900 cm^{-1}) in peroxo-species (see more details in Figure S8, Supporting Information),[9, 22] a new peak at ~ 850 cm^{-1} emerges and increases during the 4.5 V-related charging plateau, and gradually disappears with the subsequent discharge process. The potential of O-O peroxo bond appearance would be different in other systems resulting from different thermodynamic conditions, which means the environment (such as space group, neighboured atoms) surrounding oxygen atoms.[25] The reversible variation trend of the peroxo O-O bond can also be obtained on specific high voltage plateau during the 2nd cycle. The average concentration of peroxo O-O bond can be represented by relative peak area which is also shown in **Figure 3**. The relative peak area of peroxo O-O bond equals zero (means no O^--O^- bond appears) before 4.5 V-related charging plateau, then increases gradually to the maximum corresponding to the end of charging as a function of time. The area decreases to zero subsequently in discharge

process and exhibits reversible variation trend during the 2nd cycle. Moreover, according to the obtained XRD results (**Figure 2**), the formation of the newly-proposed peroxo O-O bond can be assigned to the delithiation from Li/TM layer. During charging at 4.5 V plateau, the shift of peroxo O-O stretch to higher wavenumber indicates the reduction of peroxo O-O bond length in peroxo-species.[18] The peroxo O-O bond length range can be empirically considered as 1.28 Å ~ 1.48 Å (1.28 Å in Li_2O_2 where peroxo O-O bond located at 790 cm^{-1} and 1.48 Å in H_2O_2 where peroxo O-O bond located at 878 cm^{-1})[26]. Combining with the decreasing trend of *c*-axis length during related stage (**Figure 2**), the peroxo O-O bond tends to be formed along the *c*-axis (not in *ab* plane), which is also well consistent with the mechanism proposed by related DFT simulations.[27] In this case, the causality among delithiation/lithiation between Li/TM layer, the variation of *c*-axis and the formation/decomposition of peroxo O-O bond can be rationally unified together. Consequently, essentially different from the peroxo-like $(O_2)^{n-}$-based redox process proposed by previous ex-situ XPS analysis,[11, 19, 28] herein, the operando observation and assignment of real peroxo O-O bond in peroxo-species provides new evidence for the reversible anionic redox chemistry in Li-rich cathode materials. Furthermore, the similar phenomenon in $LiPF_6$-salt electrolyte (1M in PC) can be seen in Figure S9 (see more details in Supporting Information). Moreover, X-ray photoelectron spectroscopy (XPS) etching experiment reveals that the peroxo O-O bond exists both in the surface and in the bulk (see more details in Figure S10, Supporting Information).

Besides the typical irreversible oxygen loss (such as the formation of O_2, O_2^-) in the lithium rich materials,[9, 29] herein, we demonstrate a reversible oxygen behavior with the generation of O_2^{2-} dimers, which can be sustainable in the subsequent cycle. To better understand the formation of the peroxo O-O bond during cycling, the first-principle calculations for the $Li_{1.2-x}Ni_{0.2}Mn_{0.6}O_2$ systems have

been performed. We note that the excess lithium ordering in the transition metal layer of $Li_{1.2}Ni_{0.2}Mn_{0.6}O_2$ is very complicated and a mixture of different types of local ordering.[30] However, the $Li_{1.2}Ni_{0.2}Mn_{0.6}O_2$ with honeycomb ordering of excess lithium atoms experiences an energy barrier of 1.4 eV for the formation of peroxo bonds, compared to 0.6-1 eV of Li_2MnO_3,[31] which is not realistic to occur during the room temperature cycling (see Figure S11-S13 in Supporting Information for detailed discussions). Here, we are especially interested in $Li_{1.2}Ni_{0.2}Mn_{0.6}O_2$ with local straight-type tripolymers (Figure S14), where the formation of peroxo bonds experiences no energy barrier during charging.

Thus, the $Li_{1.2}Ni_{0.2}Mn_{0.6}O_2$ crystal structure with local straight-type was built using a 5×2×1 supercell of the R$\bar{3}$m $LiMnO_2$ with partial Mn atoms replaced by Ni and Li atoms, as shown in Figure S14 (Supporting Information). Firstly, the $Li_{1.2}Ni_{0.2}Mn_{0.6}O_2$ crystal structure was relaxed, and the optimized lattice parameters of $Li_{1.2}Ni_{0.2}Mn_{0.6}O_2$ unit cell are *a*=14.49 Å, *b*= 5.81 Å and *c*=14.26 Å, respectively. Then, the crystal structures and atomic positions of the $Li_{1.2-x}Ni_{0.2}Mn_{0.6}O_2$ systems during the whole charging processes were relaxed, and the corresponding charge density distributions for *x* = 0.6, 0.7, 0.8, 0.9, 1.0 and 1.1 were shown in **Figure 4**. During the initial charging process (*x* from 0 to 0.6), some lithium atoms in lithium layers are preferentially divorced from the $Li_{1.2-x}Ni_{0.2}Mn_{0.6}O_2$ cathode. No peroxo O-O bond is observed during this initial charging period. When reaching the middle period (i.e., *x*=0.7), some excess lithium atoms in the TM-layers begin to leave from $Li_{0.5}Ni_{0.2}Mn_{0.6}O_2$ cathode, and two adjacent O atoms of the MnO_6 octahedron near the excess lithium vacancies get closer to each other. Moreover, remarkable electrons between these two closer O atoms can be observed (yellow isosurfaces in black dotting circles), demonstrating the formation of O-O covalent bond, and the corresponding O-O bond length is calculated to be 1.343 Å

(**Table 1**), which is much shorter than 2.6 Å of interatomic distance between adjacent O atoms in MnO_6 octahedrons, and even shorter than 1.49 Å of the peroxo O-O bond length in Li-Rich Li_2MnO_3 system[31]. According to the Bader charge data (Figure S15, Supporting Information), the O atomic charges of the special O-O bond in $Li_{0.5}Ni_{0.2}Mn_{0.6}O_2$ cathode are larger than those in $Li_{0.6}Ni_{0.2}Mn_{0.6}O_2$ and other O atoms far from the excess lithium vacancies. All these evidence indicate the formation of the peroxo O-O bond between x = 0.6 and 0.7, corresponding to the specific capacity between 190 and 220 mA h g^{-1}, which is consistent with the in-situ Raman spectra data. During the final charging period (x= 0.8 to 1.1), more and more peroxo O-O bonds form with smaller bond lengths and more positive O atomic charges, which is also consistent with the variation trend of Raman shift and relative peak area of O-O bonds in our in-situ Raman spectra data.

The processes summarizing the aforementioned discussion are as follows: At first, Li^+ migrates out from Li layers with the charge compensation by $Ni^{2+/4+}$ redox couple, corresponding to ~ 130 mA h g^{-1}. From then on, oxidation of oxygen starts to emerge for charging compensation till the end of the charging because Ni^{2+} is totally oxidized to Ni^{4+} and Mn^{4+} can't be oxidized to a higher valence state in octahedral site.[32] Afterwards, the oxidation of oxygen are the main responsible for charge compensation at the plateau of ~ 4.5 V. Since about 1.1 Li^+ can be extracted from the structure, Li^+ continues to be removed out from Li layers and TM layers accompanied with appearance of peroxo O-O bond. The cooperative effect of anionic redox and extraction of Li^+ leads to the smooth change of c-lattice parameter and eventually turns it back to a lower value at this process. Figure S16 (Supporting Information) shows the participation of Ni^{2+} and oxygen involvement during the charging process. The charge compensation during discharging process is similar with charging process. The changes of c-lattice parameter shows a cooperation including the reversible anionic (O^-

/O^{2-}) redox process, the reduction of Ni and the reinsertion of Li^+ into the structure. Moreover, combining the changes of peroxo O-O bond length in Raman results with the variation tendency of *c*-axis length in XRD results, the formation of peroxo O-O bond is speculated along the *c*-axis, which is also confirmed by the DFT calculations.

In summary, the typical Li-rich positive material $Li_{1.2}Ni_{0.2}Mn_{0.6}O_2$ was systematically studied. Based on the advanced in-situ technologies, we can directly visualize the structural evolution accompanied by the (de)lithiation, including the reversible anionic redox process, even peroxo O-O bond formation and extinction along *c* axis, which are consistent well with the DTF calculations. What's more, both cationic and anionic redox processes are reversible even in subsequent cycles, enabling Li-rich layered oxides a high capacity. Our findings highlight a new evidence for the reversible anionic redox process in Li-rich cathode materials, and provide a deep understanding of intercalation chemistry and new insights into the design of high-performance Li-rich layered oxides.

Supporting Information

Supporting Information is available from the Wiley Online Library or from the author.

Acknowledgements

Xiang Li and Yu Qiao contributed equally to this work. Xiang Li is grateful for financial support of the CSC (China Scholarship Council) scholarship. This work was partially supported financially by National Basic Research Program of China (2014CB932302, 2014CB932303), Natural Science Foundation of Jiangsu Province of China (BK20170630), the Fundamental Research Funds for the Central Universities (021314380076, 021314380080), the National Natural Science Foundation of China (21673116, 2163303), and the Natural Science Foundation of Jiangsu Province of China

(BK20160068). We are very grateful to Prof. Ying Shirley Meng and Prof. Shou-Hang Bo for the discussion.

Received: ((will be filled in by the editorial staff))
Revised: ((will be filled in by the editorial staff))
Published online: ((will be filled in by the editorial staff))

References

[1] a) J. B. Goodenough, Y. Kim, *Chem. Mater.* **2010**, *22*, 587; b) M. S. Whittingham, *Chem. Rev.* **2004**, *104*, 4271; c) A. S. Arico, P. Bruce, B. Scrosati, J. M. Tarascon, W. Van Schalkwijk, *Nat. Mater.* **2005**, *4*, 366; d) J. M. Tarascon, M. Armand, *Nature* **2001**, *414*, 359; e) P. He, H. J. Yu, D. Li, H. S. Zhou, *J. Mater. Chem.* **2012**, *22*, 3680.

[2] a) Z. D. Huang, X. M. Liu, B. A. Zhang, S. W. Oh, P. C. Ma, J. K. Kim, *Scr. Mater.* **2011**, *64*, 122; b) Y. Jiang, H. Zhuang, Q. L. Ma, Z. Jiao, H. J. Zhang, R. Z. Liu, Y. L. Chu, B. Zhao, *J. Mater. Res.* **2013**, *28*, 1505; c) S. Y. Yang, X. Y. Wang, X. K. Yang, L. Liu, Z. L. Liu, Y. S. Bai, Y. P. Wang, *J. Solid State Electrochem.* **2012**, *16*, 1229; d) L. J. Xi, C. W. Cao, R. G. Ma, Y. Wang, S. L. Yang, J. Q. Deng, M. Gao, F. Lian, Z. G. Lu, C. Y. Chung, *Phys. Chem. Chem. Phys.* **2013**, *15*, 16579.

[3] J. S. Kim, C. S. Johnson, J. T. Vaughey, M. M. Thackeray, S. A. Hackney, *Chem. Mater.* **2004**, *16*, 1996.

[4] D. L. Ye, G. Zeng, K. Nogita, K. Ozawa, M. Hankel, D. J. Searles, L. Z. Wang, *Adv. Funct. Mater.* **2015**, *25*, 7488.

[5] Y. D. Wang, J. W. Jiang, J. R. Dahn, *Electrochem. Commun.* **2007**, *9*, 2534.

[6] H. J. Yu, Y. G. So, A. Kuwabara, E. Tochigi, N. Shibata, T. Kudo, H. S. Zhou, Y. Ikuhara, *Nano Lett.* **2016**, *16*, 2907.

[7] a) M. M. Thackeray, C. S. Johnson, J. T. Vaughey, N. Li, S. A. Hackney, *J. Mater. Chem.* **2005**, *15*, 2257; b) Z. H. Lu, D. D. MacNeil, J. R. Dahn, *Electrochem. Solid-State Lett.* **2001**, *4*, A191.

[8] C. S. Johnson, J. S. Kim, C. Lefief, N. Li, J. T. Vaughey, M. M. Thackeray, *Electrochem. Commun.* **2004**, *6*, 1085.

[9] K. Luo, M. R. Roberts, R. Hao, N. Guerrini, D. M. Pickup, Y. S. Liu, K. Edstrom, J. H. Guo, A. V. Chadwick, L. C. Duda, P. G. Bruce, *Nat. Chem.* **2016**, *8*, 684.

[10] D. H. Seo, J. Lee, A. Urban, R. Malik, S. Kang, G. Ceder, *Nat. Chem.* **2016**, *8*, 692.

[11] M. Sathiya, G. Rousse, K. Ramesha, C. P. Laisa, H. Vezin, M. T. Sougrati, M. L. Doublet, D. Foix, D. Gonbeau, W. Walker, A. S. Prakash, M. Ben Hassine, L. Dupont, J. M. Tarascon, *Nat. Mater.* **2013**, *12*, 827.

[12] E. McCalla, A. M. Abakumov, M. Saubanere, D. Foix, E. J. Berg, G. Rousse, M. L. Doublet, D. Gonbeau, P. Novak, G. Van Tendeloo, R. Dominko, J. M. Tarascon, *Science* **2015**, *350*, 1516.

[13] K. A. Jarvis, Z. Q. Deng, L. F. Allard, A. Manthiram, P. J. Ferreira, *Chem. Mater.* **2011**, *23*, 3614.

[14] a) A. C. Larson, R. B. Von Dreele, *Los Alamos Natl. Lab. Rep. LAUR* **1994**, 86; b) B. H. Toby, *J. Appl. Crystallogr.* **2001**, *34*, 210.

[15] Z. H. Lu, J. R. Dahn, *J. Electrochem. Soc.* **2002**, *149*, A1454.

[16] a) L. Zhang, H. Noguchi, *J. Electrochem. Soc.* **2003**, *150*, A601; b) Z. H. Lu, L. Y. Beaulieu, R. A. Donaberger, C. L. Thomas, J. R. Dahn, *J. Electrochem. Soc.* **2002**, *149*, A778.

[17] D. Mohanty, S. Kalnaus, R. A. Meisner, K. J. Rhodes, J. L. Li, E. A. Payzant, D. L. Wood, C. Daniel, *J. Power Sources* **2013**, *229*, 239.

[18] J. M. Tarascon, G. Vaughan, Y. Chabre, L. Seguin, M. Anne, P. Strobel, G. Amatucci, *J. Solid State Chem.* **1999**, *147*, 410.

[19] P. E. Pearce, A. J. Perez, G. Rousse, M. Saubanere, D. Batuk, D. Foix, E. McCalla, A. M. Abakumov, G. Van Tendeloo, M. L. Doublet, J. M. Tarascon, *Nat. Mater.* **2017**, *16*, 850.

[20] B. Qiu, M. H. Zhang, Y. G. Xia, Z. P. Liu, Y. S. Meng, *Chem. Mater.* **2017**, *29*, 908.

[21] Y. Qiao, S. Wu, J. Yi, Y. Sun, S. Guo, S. Yang, P. He, H. Zhou, *Angew. Chem. Int. Ed.* **2017**, *56*, 4960.

[22] Y. Qiao, S. Ye, *J. Phys. Chem. C* **2015**, *119*, 12236.

[23] J. F. Li, Y. F. Huang, Y. Ding, Z. L. Yang, S. B. Li, X. S. Zhou, F. R. Fan, W. Zhang, Z. Y. Zhou, D. Y. Wu, B. Ren, Z. L. Wang, Z. Q. Tian, *Nature* **2010**, *464*, 392.

[24] P. Lanz, C. Villevieille, P. Novak, *Electrochim. Acta* **2014**, *130*, 206.

[25] a) M. Sathiya, A. M. Abakumov, D. Foix, G. Rousse, K. Ramesha, M. Saubanere, M. L. Doublet, H. Vezin, C. P. Laisa, A. S. Prakash, D. Gonbeau, G. VanTendeloo, J. M. Tarascon, *Nat. Mater.* **2015**, *14*, 230; b) T. Ohzuku, A. Ueda, M. Nagayama, *J. Electrochem. Soc.* **1993**, *140*, 1862; c) S. H. Park, S. W. Oh, S. H. Kang, I. Belharouak, K. Amine, Y. K. Sun, *Electrochim. Acta* **2007**, *52*, 7226; d) N. Yabuuchi, K.

Kubota, M. Dahbi, S. Komaba, *Chem. Rev.* **2014**, *114*, 11636; e) M. Guignard, C. Didier, J. Darriet, P. Bordet, E. Elkaïm, C. Delmas, *Nat. Mater.* **2013**, *12*, 74.

[26] a) A. J. Bridgeman, J. Rothery, *J. Chem. Soc. Dalton Trans.* **1999**, 4077; b) Z. X. Liu, L. R. De Jesus, S. Banerjee, P. P. Mukherjee, *ACS Appl. Mater. Interfaces* **2016**, *8*, 23028.

[27] M. Saubanere, E. McCalla, J. M. Tarascon, M. L. Doublet, *Energy Environ. Sci.* **2016**, *9*, 984.

[28] D. Foix, M. Sathiya, E. McCalla, J. M. Tarascon, D. Gonbeau, *J. Phys. Chem. C* **2016**, *120*, 862.

[29] a) A. R. Armstrong, M. Holzapfel, P. Novak, C. S. Johnson, S. H. Kang, M. M. Thackeray, P. G. Bruce, *J. Am. Chem. Soc.* **2006**, *128*, 8694. b) S. Hy, F. Felix, J. Rick, W. N. Su, B. J. Hwang, *J. Am. Chem. Soc.* **2014**, *136*, 999.

[30] a) K. Luo, M. R. Roberts, N. Guerrini, N. Tapia-Ruiz, R. Hao, F. Massel, D. M. Pickup, S. Ramos, Y. S. Liu, J. Guo, *J. Am. Chem. Soc* **2016**, *138*, 11211; b) M. Gu, I. Belharouak, A. Genc, Z. Wang, D. Wang, K. Amine, F. Gao, G. Zhou, S. Thevuthasan, D. R. Baer, *Nano Lett.* **2012**, *12*, 5186; c) M. M. Thackeray, S. H. Kang, C. S. Johnson, J. T. Vaughey, R. Benedek, S. Hackney, *J. Mater. Chem.* **2007**, *17*, 3112.

[31] H. R. Chen, M. S. Islam, *Chem. Mater.* **2016**, *28*, 6656.

[32] J. Roos, C. Eames, S. M. Wood, A. Whiteside, M. S. Islam, *Phys. Chem. Chem. Phys.* **2015**, *17*, 22259.

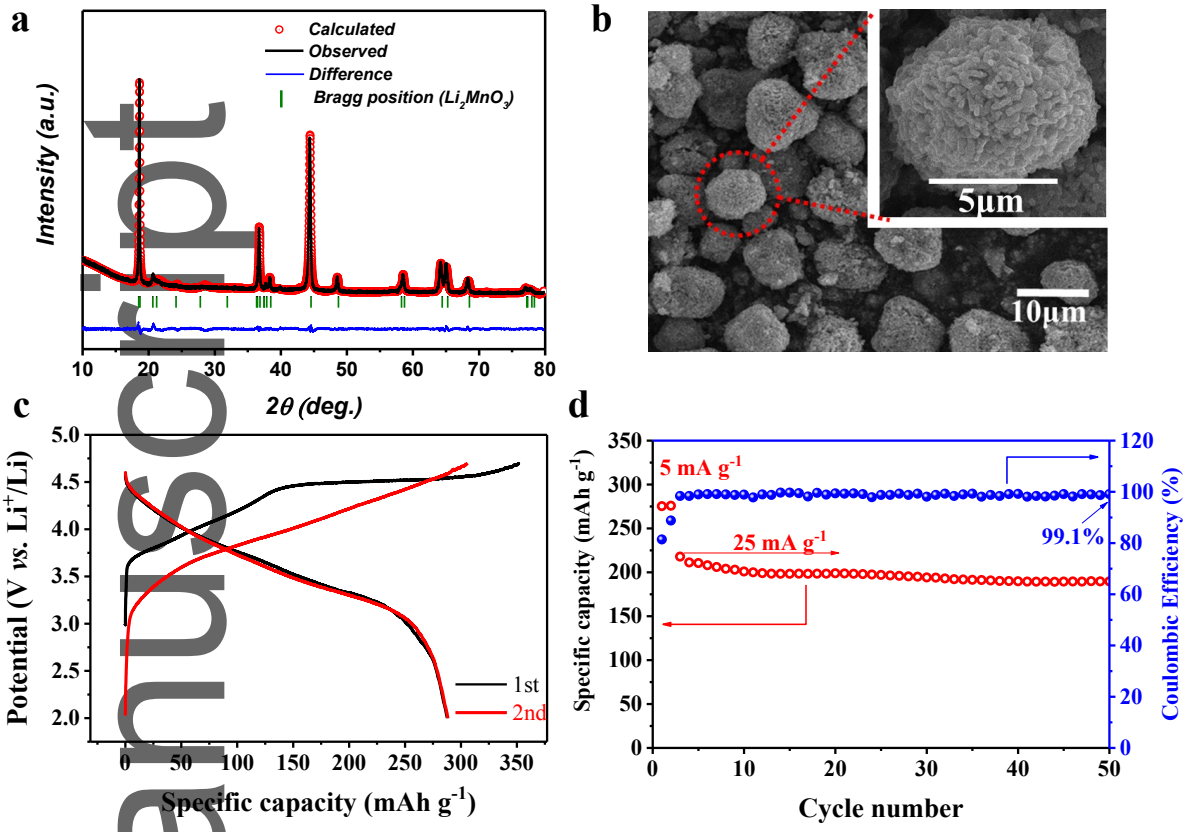

Figure 1. XRD, SEM and electrochemical characterizations of $Li_{1.2}Ni_{0.2}Mn_{0.6}O_2$. a) XRD patterns of $Li_{1.2}Ni_{0.2}Mn_{0.6}O_2$ and Rietveld refinement. b) SEM images of $Li_{1.2}Ni_{0.2}Mn_{0.6}O_2$. The inset shows zoom in image of the particle in red dotted line. c) Typical charge-discharge profiles between 2.0 and 4.7 V at 5 mA g^{-1}. d) The cycling performance with coulombic efficiency at 5 mA g^{-1}(first two cycles) and 25 mA g^{-1}(subsequent cycles).

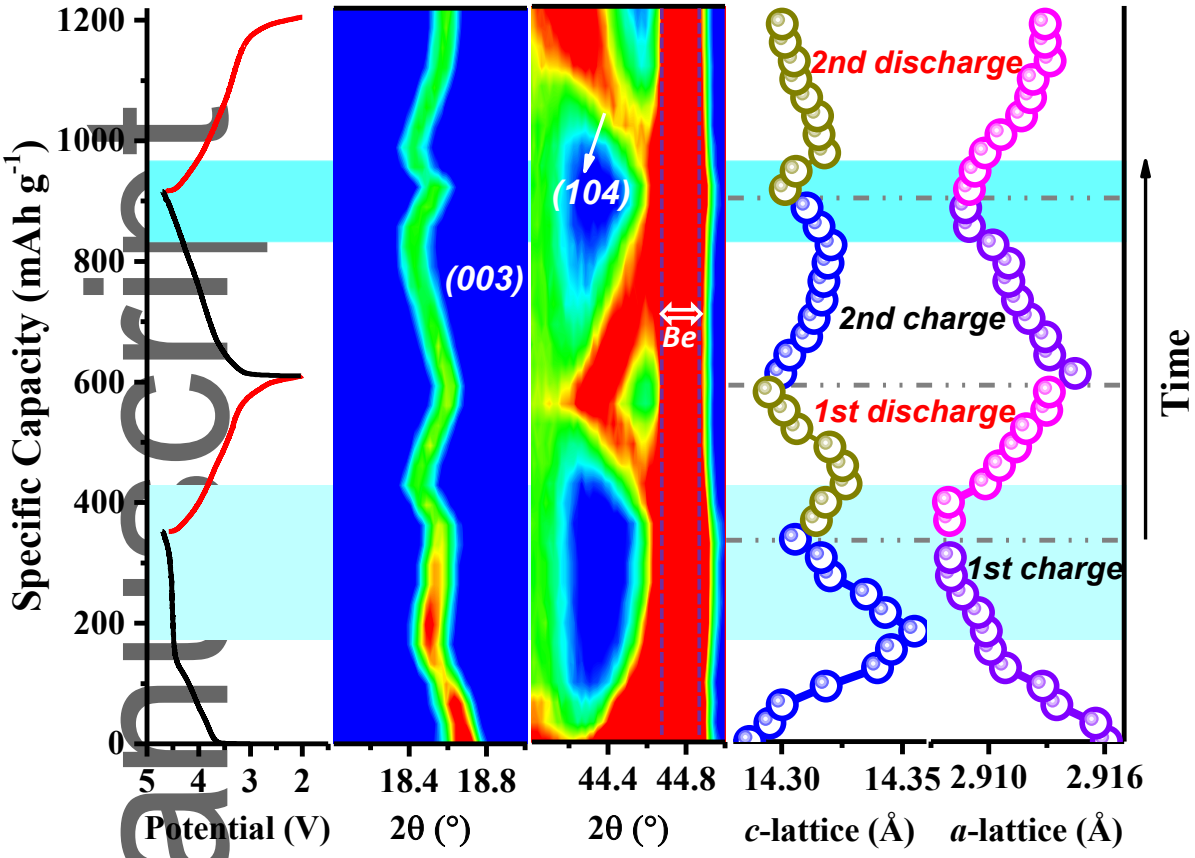

Figure 2. Color-coded images of the peak (003) and (104), refined *c*-lattice, and *a*-lattice parameters during initial two cycles. The range of intensity distribution plots with reference color bar is from 3000 to 5000.

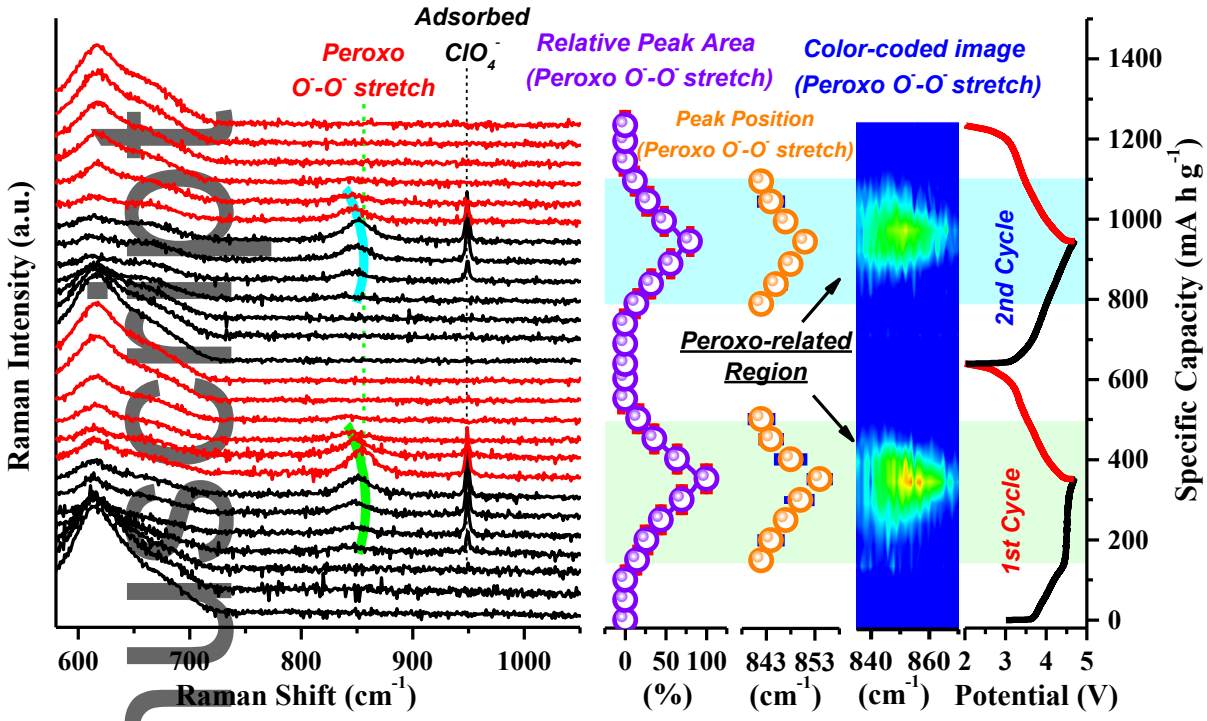

Figure 3. Capacity dependent in situ Raman spectra recorded during initial two galvanostatic cycles (5 mA g^{-1}). The novel peroxo-species peak has been highlighted, and corresponding capacity dependence of peak area (purple hollow), peak position (orange hollow) and color-coded image are summarized, respectively. The range of intensity distribution plots with reference color bar is from 0 to 0.03.The related voltage profiles are shown for clarity.

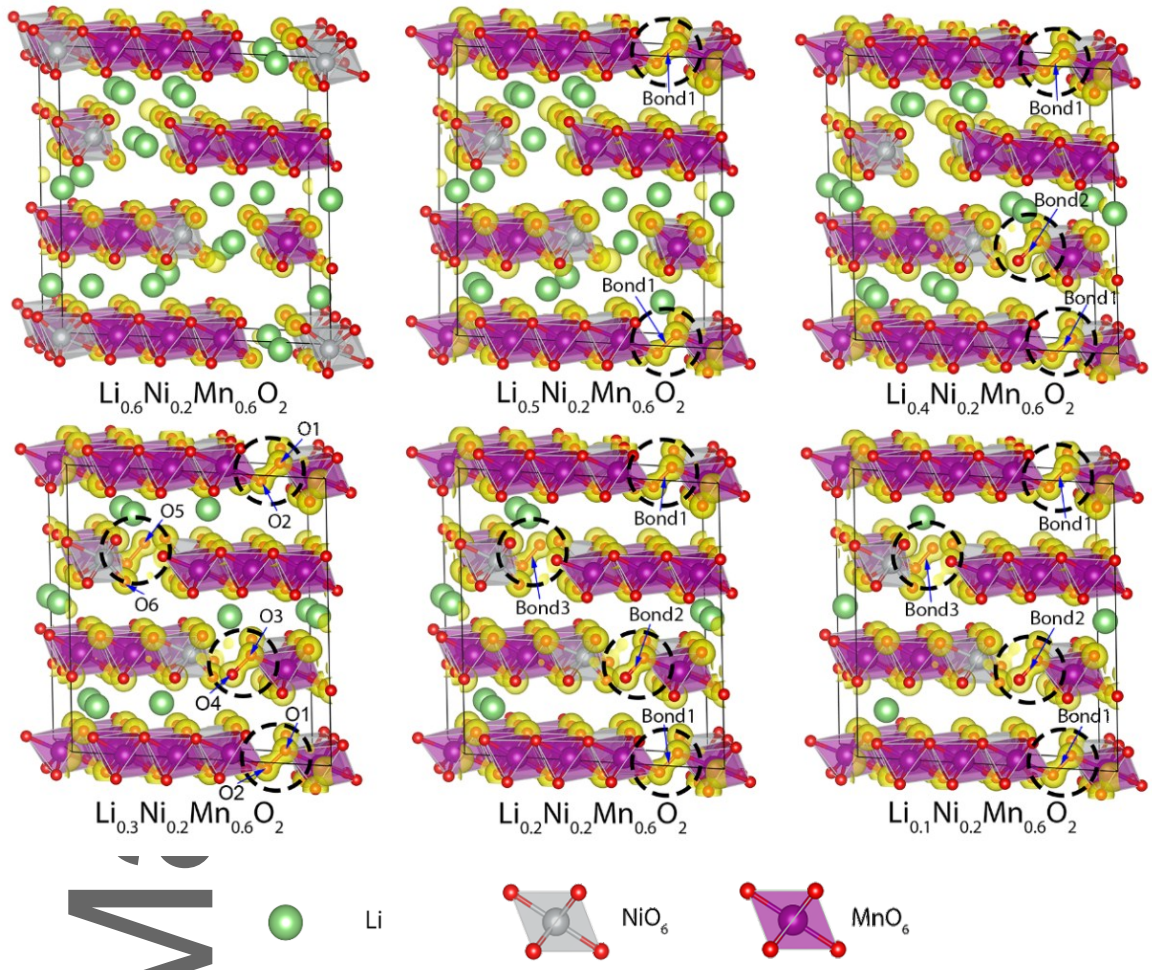

Figure 4. Charge density distributions (yellow isosurfaces = 0.2 e Å^{-3}) of the $Li_{1.2-x}Ni_{0.2}Mn_{0.6}O_2$ systems (x = 0.6, 0.7, 0.8, 0.9, 1.0 and 1.1) with peroxo O-O bonds (in black dotting circles) during the charging and discharging processes.

Table 1. The peroxo O-O bond length (in Å) of the $Li_{1.2-x}Ni_{0.2}Mn_{0.6}O_2$ systems (x = 0.6, 0.7, 0.8, 0.9, 1.0 and 1.1) during the charging and discharging processes

	O-O bond1	O-O bond2	O-O bond3
$Li_{0.6}Ni_{0.2}Mn_{0.6}O_2$	\	\	\

$Li_{0.5}Ni_{0.2}Mn_{0.6}O_2$	1.343	\	\
$Li_{0.4}Ni_{0.2}Mn_{0.6}O_2$	1.315	1.415	\
$Li_{0.3}Ni_{0.2}Mn_{0.6}O_2$	1.314	1.348	1.350
$Li_{0.2}Ni_{0.2}Mn_{0.6}O_2$	1.306	1.308	1.341
$Li_{0.1}Ni_{0.2}Mn_{0.6}O_2$	1.305	1.307	1.310

A typical Li-rich material $Li_{1.2}Ni_{0.2}Mn_{0.6}O_2$ is systematically analyzed by in-situ X-ray diffraction (XRD) and Raman spectroscopy. We directly visualize peroxo O-O bonding mostly along the *c*-axis and demonstrate reversible O^{2-}/O^{-} redox process. Additionally, the formation of peroxo O-O bond is calculated via the density functional theory (DFT), and the corresponding O-O bond length of ~1.3 Å matches well with in-situ Raman results. These findings enrich the oxygen chemistry in layered oxides and open opportunities for the design of high-performance cathode materials for lithium-ion batteries.

Keyword: Li-ion batteries, Li-rich material, oxygen redox, in-situ XRD, in-situ Raman

Xiang Li, Yu Qiao, Shaohua Guo,* Zhenming Xu, Hong Zhu, Xiaoyu Zhang, Yang Yuan, Ping He,* Masayoshi Ishida, and Haoshen Zhou*

Direct visualization of reversible O^{2-}/O^{-} redox process in Li-rich cathode materials